An active source seismo-acoustic experiment using tethered balloons to validate instrument concepts and modelling tools for atmospheric seismology

R. F. Garcia, L. Martire, Y. Chaigneau, A. Cadu, D. Mimoun, M. Bassas Portus, A. Sournac, M. Sylvander, H. Pauchet, S. Benahmed, et al.

Geophysical Journal International

Geophys. J. Int. (2021) **225,** 186–199
Advance Access publication 2020 December 12
GJI Seismology

doi: 10.1093/gji/ggaa589

An active source seismo-acoustic experiment using tethered balloons to validate instrument concepts and modelling tools for atmospheric seismology

R. F. Garcia[1], L. Martire,[1] Y. Chaigneau,[1] A. Cadu,[1] D. Mimoun,[1] M. Bassas Portus,[1] A. Sournac,[1] M. Sylvander,[2] H. Pauchet,[2] S. Benahmed[2] and R. Martin[3]

[1]*Institut Supérieur de l'Aéronautique et de l'Espace SUPAERO,* 10 *Avenue Edouard Belin,* 31400 *Toulouse, France. E-mail: raphael.garcia@isae.fr*
[2]*Institut de Recherche en Astrophysique et Planétologie, Université Toulouse III Paul Sabatier, CNRS, CNES,* 14 *Av. E. Belin,* 31400, *Toulouse, France*
[3]*Géosciences Environnement Toulouse (GET), Observatoire Midi-Pyrénées (OMP),* 14 *Avenue Edouard Belin, Toulouse* 31400, *France*

Accepted 2020 November 29. Received 2020 November 28; in original form 2020 April 29

SUMMARY

The measurements of acoustic waves created by a quake are of great interest for planets with hot and dense atmospheres, like Venus, because surface deployments of seismometers will last only a few hours, whereas freeflying balloons could fly many days. Infrasound sensors can also be used to constrain subsurface properties during active seismic experiments. This study presents a controlled source seismo-acoustic experiment using infrasonic sensors and accelerometers mounted on a tethered helium balloon. Both the acoustic waves generated below the balloon by seismic surface waves, and the ones generated by strong ground motions above the seismic source are clearly observed and separated on the records of the various instruments. This data set allows various validations and investigations. First, it validates the ground to air coupling theory and our numerical modelling tools. Then, it allows us to demonstrate that antenna processing of infrasound sensors deployed below the balloon can estimate the arrival incidence angle of the acoustic waves within 10°. Finally, a polarization analysis of the accelerometers taped on the balloon envelope is presented. It demonstrates that accelerometer records are strongly dependent on their location on the balloon due to its deformations and rotations. However, the different acoustic signals can be distinguished through their polarization, and a best sensor location is estimated at the bottom of the balloon envelope. These results are a first step towards detecting and locating seismic activity using airborne acoustic sensors on Venus and elsewhere. However, some observations of earthquake signals in a more realistic geometry are still missing.

Key words: Numerical modelling; Planetary interiors; Computational seismology; Controlled source seismology; Seismic instruments.

1 INTRODUCTION

Ground to air mechanical couplings of the solar system planets is an active research area since the earliest measurements of atmospheric waves generated by seismic surface waves (Hines 1960). The deployment of various observations systems of the Earth's ionosphere and thermosphere since 1980 allowed to clearly observe the atmospheric acoustic and gravity waves created by quakes, tsunamis and volcanoes (Lognonné 2009). In parallel, various modelling tools have been developed from coupled solid/atmosphere normal modes (Lognonné *et al.* 1998) to full numerical tools coupling the seismic waves to a nonlinear windy atmosphere (Brissaud 2017; Sabatini *et al.* 2019), some of these including also the coupling with the atmospheric plasma (Kherani *et al.* 2009; Zettergren & Snively 2015; Zettergren *et al.* 2017).

The infrasonic signals associated to underground explosions were detected by different aerial platforms using parachutes (Banister & Hereford 1982, 1991) and balloons (Bowman *et al.* 2014). Banister & Hereford (1982) reported in particular seismic surface waves detected below a parachute after a large underground explosion. Whereas Bowman *et al.* (2014) describe the infrasonic signals generated buried explosions simulating volcanoes from infrasound sensors below balloons. This study underlines the difficulty to separate acoustic waves created by ground movements from the ones induced by venting.

The acoustic signals created by ground movements radiate their energy preferentially upward (Arrowsmith *et al.* 2012). That's why

infrasound sensors deployed on balloon platforms provide the best view point to detect and characterize these waves. Such measurements already demonstrated their interest to characterize the sources of microbaroms and microseismic signals above the ocean (Bowman & Lees 2017, 2019; Poler *et al.* 2020). When applied to active seismic experiments, these measurements are providing additional informations on the source and its coupling with the ground (Young *et al.* 2018). In addition, the seismo-acoustic waves are very sensitive to the presence of soft subsurface structures in which the seismic waves propagate slower than the sound (Martire *et al.* 2018). The use of infrasounds created by quakes and volcanoes may also allow to infer the atmosphere structure from these well-known infrasonic sources (Pichon 2005) or to determine quake parameters assuming a known atmospheric structure (Averbuch *et al.* 2020).

Even if the Earth's observations of atmospheric perturbations generated by tectonic events are numerous, their interest for Earth's internal structure imaging is limited because the seismometers have a much lower noise level than atmospheric observables. Thus, atmospheric observations with good signal-to-noise ratio that can complement ground sensors concern mainly oceanic regions and signals with large amplitude and periods longer than 100 s. However, concerning planets with hot and dense atmosphere, the science interest for internal structure imaging is strong (Lognonné & Johnson 2007). Two main reasons are driving this interest. First, long-lived ground deployment and proper noise levels are difficult to demonstrate for surface seismometers. Then, the solid/atmosphere mechanical coupling is much stronger than on Earth, generating atmospheric signals with larger amplitude (Garcia *et al.* 2005). And finally a single seismic surface wave train contains a large amount of information in its dispersion, without requiring quake location (Lognonné *et al.* 2016).

The Venus case has been quite extensively studied (Stevenson *et al.* 2015). Various observation methods are suggested for this planet. From top to bottom in the atmosphere, day time ionosphere electron density variations (Lognonné *et al.* 2016), day time non Local Thermodynamic Equilibrium (non-LTE) CO_2 emissions at 4.3 μm (Garcia *et al.* 2009), night time O_2 airglow emissions at 1.27 μm (Didion *et al.* 2018) and pressure sensors on balloon platforms (Stevenson *et al.* 2015) have been suggested.

Various Earth's demonstrator experiments have been set up in the recent years to investigate the capabilities of pressure and accelerometer sensors on tethered and free air balloons platforms to measure acoustic waves generated by ground shaking (Bowman *et al.* 2018; Krishnamoorthy *et al.* 2018, 2019). There is various returns from these experiments. First the relative wind between balloon platform and the sensors is main noise source. This relative wind is much lower for freeflying balloons than for tethered balloons, recent stratospheric experiments even suggest that wind protection systems are not improving the noise floor of pressure records (Krishnamoorthy *et al.* 2020). Parameters like source scaling, subsurface seismic velocities, air temperature and wind, as well as experiment geometry are also critical to ensure a proper observation and analysis of the acoustic waves created by ground movements.

Thanks to these early results, we designed an experiment with the following objectives. First, to observe the acoustic emissions of the seismic surface waves passing below the balloon, which is the signal expected for planetary atmospheric seismology. Then, to demonstrate the capability of the antenna processing of infrasound sensors, and of the accelerometers attached to the balloon envelope, to determine the arrival direction of the infrasounds. And finally, to benchmark our numerical modelling tools with a real experiment.

Next section describes the experiment. The results are then presented, through various analysis of the clear acoustic, accelerometric and seismic signals generated by the seismic sources. We conclude on the interest of such observations to demonstrate the planetary observation case, and the remaining efforts to be deployed.

2 EXPERIMENT DESCRIPTION

2.1 Science objectives

The main objective of the experiment is to demonstrate that infrasound sensors deployed on a balloon platform can record infrasonic waves generated by seismic waves. We target in particular the infrasounds generated by seismic surface waves just below the balloon. Secondary objectives of the experiment are:

(i) to demonstrate that antenna processing using two infrasound sensors deployed at different altitudes below the balloon allows to recover the incidence angle of infrasonic waves;

(ii) to investigate the capability of accelerometers mounted on balloon envelope to determine the arrival direction of incoming infrasonic waves;

(iii) to validate our numerical simulation tools of solid–atmosphere coupling with real data.

In order to reach these objectives, the experiment was located on an hard rock quarry to ensure that the seismic waves propagate faster than the infrasounds. This setting is critical to obtain the atmospheric infrasound head wave following the seismic surface wave train (Martire *et al.* 2018). Two dedicated explosives shots were performed at 25 m depth to excite seismic waves. Seismic and infrasonic waves were recorded on the ground by various sensor types (seismometers, microphones and infrasound sensors) in order to characterize seismic and infrasonic waves. In addition, two infrasound sensors are deployed below a low altitude tethered balloon and some accelerometers are taped on its envelope. Finally, the experiment optimal geometry was determined by using numerical simulations (Martire *et al.* 2018) in order to ensure signal amplitudes large enough on the infrasound sensors to be above their noise level, and small enough on the seismic sensors to be below their saturation limit.

2.2 Experiment setup

The experiment was conducted in the GAIA limestone quarry, property of COLAS company, located in South of France close to the town of Glanes. Fig. 1 describes the geometry of the experiment. We used a field with a low slope at the top of the quarry to deploy our ground sensors and our tethered balloon. The soft soil layer on top of hard rock has a thickness going from zero at the shot locations to 80 cm in the balloon deployment area. All ground sensors were installed in holes at the surface of the hard rock layer.

A seismic line, composed of triaxial Guralp CMG40-T seismometers, is deployed every 50 m along azimuth 262.83° (clockwise from North from the second shot location). At the end of this line, 190 m from the shots, a small seismic array forming a cross is deployed with a Trillium Compact 120 (TC120) seismometer in the middle of the cross. At the same location, two microphones (Earthworks M30BX models) are deployed, respectively, one metre before and after the TC120 seismometer along the seismic line. A spare model of our balloon infrasound instruments is also deployed on the ground one meter away from the TC120 seismometer. Infrasound

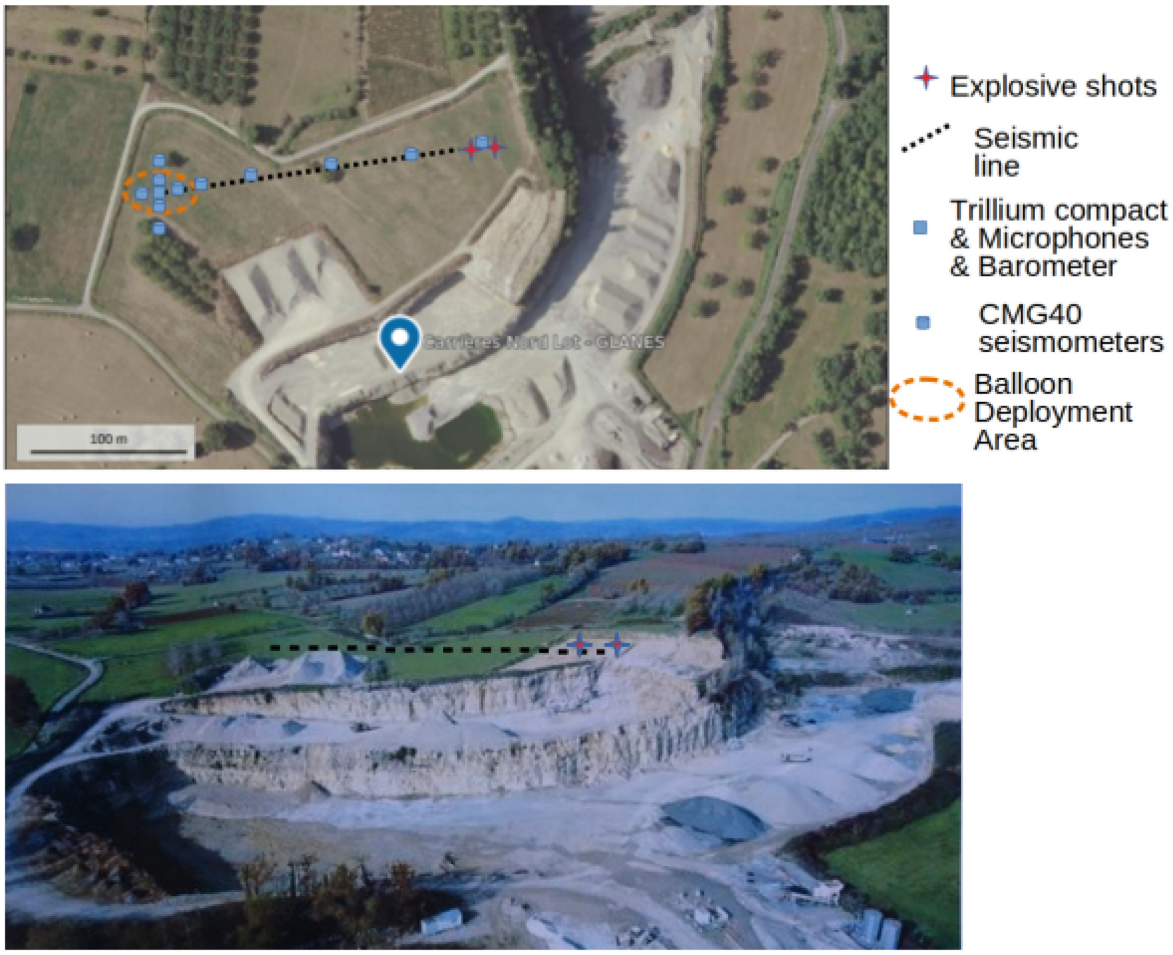

Figure 1. On the top: view from the top of the experiment setup indicating the positions of the shots, the various sensors and the balloon location. On the bottom: aerial view of quarry showing the shots location and the topography.

instruments are identical to the ones described by Krishnamoorthy *et al.* (2018), using Paroscientific sensors recording absolute pressure at 100 samples per seconds (sps). These instruments also contain a GPS receiver sampled at 1 sps.

The balloon platform is a 7-m long helium balloon deployed at 90 m altitude at approximately 200 m horizontal distance from the shots. Four of the Inertial Measurement Units (IMU, YEI 3-Space Sensor model) were taped to the balloon's envelope: at its nose, tail, top and bottom. However, only the nose, tail and bottom ones collected data of the two shots, the others turning off earlier due to battery shortage. Infrasound instruments were deployed, respectively, 1 and 45 m below the balloon envelope. Fig. 2 assembles pictures showing the experiment's setup.

Two underground explosive shots were performed, both based on an emulsion of ammonium nitrate (NH_4NO_3). The commercial reference for the unit cartridges we used is 'Emulstar 8000UG'. Their theoretical yield is exactly equivalent to TNT. The shots of 25 and 50 kg of net explosive mass (NEM) were located at two different positions, respectively at the origin of the seismic line and 11 m away in direction of seismic sensors. The explosives were buried in a borehole down to 25 m depth, filling the hole respectively over 3.2 and 6.4 m in the vertical direction. An hall effect current meter, clamped on the electric line commanding the shots allowed to obtain a precise timing of the explosions. A comparison of shot timing with seismic records indicates that the proper signal to track on the electric line is when the current is coming back to zero due to the break of the line by the shot. We estimate the uncertainty on this timing to be around 2 ms.

2.3 Experiment description

The experiment was conducted on 2018 November 9. All the sensors were deployed during the morning. The first shot (25 kg, 25 m depth) was fired at 11:15:02.985 (UTC) and the second one (50 kg, 25 m depth) was fired at 13:34:22.155 (UTC). Weather conditions were excellent with an almost zero wind speed, and thus very low wind noise on infrasound instruments. Infrasound instruments are providing a record of the absolute pressure. These instruments also measure the air temperature from the ground up to the balloon altitude. From the temperatures recorded at the time of the first shot (21.9, 20.3 and 18.8 °C at respectively 0.0, 29.0 and 66.0 m altitude above ground level), we estimate the speed of sound using the formula for dry air (see Appendix A) to be 345.12 m s^{-1} at ground level and 343.3 m s^{-1} at balloon altitude. The shot signals were recorded by all sensors, except some IMU sensors which ran out of batteries. The recordings from the seismic sensors located within 70 m of the shots were barely usable due to the signal saturation induced by the strong ground motions. Despite the 11 m position difference in source location, the records of the two shots by the

Figure 2. Left: picture taken from shot zone and looking towards the ground instrument line (marked by holes in the ground) and balloon deployment. Middle: balloon, showing upper infrasound sensor and two IMUs taped on envelope at the nose and the bottom of the balloon. Right: balloon and tethering system, showing the two identical infrasound sensors attached to the balloon platform. One at the bottom of the image (40 m below the balloon) and one attached just below the balloon (better seen in the middle image).

same sensors have almost identical waveforms. Their amplitude is scaling linearly with NEM.

3 RESULTS

3.1 Seismic investigations

Seismic velocities were determined with time–distance plots. Fig. 3 presents time–distance plots of the vertical component of the seismic records, bandpass filtered in different bands for *P* and surface wave investigations. Since no breaking of slopes is observed, no major discontinuities are detected by this seismic refraction method, suggesting a sufficient thickness of the hard rock layer. The *P* and surface wave velocities are estimated at 3950 ± 500 and 1580 ± 300 m s^{-1} in agreement with literature estimates for limestone (Bourbié *et al.* 1987, table 5.2).

3.2 Seismic to acoustic wave conversion

Fig. 4 compares ground motions and pressure perturbations right above the ground. The microphones have a high-pass transfer function above 9 Hz and the infrasound instruments have a low-pass transfer function below 30 Hz, thus the 10–30 Hz frequency range is covered by both instruments. In this frequency range a high seismic energy is emitted by the shots. Pressure records of the different sensors (on top of Fig. 4) are very similar if we exclude calibration uncertainties of microphones below 10 Hz. The sensitivity of the microphones to ground velocities at 20 Hz is estimated lower than 0.01 Pa (mm s^{-1})$^{-1}$ by Sylvander *et al.* (2007). The sensitivity of the infrasound sensors in the same frequency range is estimated lower than 0.4 Pa (m s^{-1} s^{-1})$^{-1}$ from Paroscientific data sheet. From the measured ground movements, the contamination of pressure measurements by movements of the sensors is estimated below 0.04 Pa from microphones, and below 0.2 Pa for infrasound sensors, whereas the measured pressure variations are of the order of 1 Pa amplitude. The seismo-acoustic conversion of vertical ground velocity (V_z) into atmospheric pressure perturbation (ΔP) is estimated using the impedance relation linking the particle velocity to the pressure perturbation in an acoustic wave: $\Delta P = (\rho_a c)V_z$. We simply assume here that the vertical ground movement is forcing the acoustic particle velocity in the atmosphere. This seismo-acoustic conversion is predicting both the amplitude and the waveform of the first pressure perturbation (between 0.1 and 0.3 s after the shot). The atmospheric density (ρ_a) and sound speed (c) are deduced from the external temperature measurements performed during the experiment. The close match of the measured waveforms to the ones predicted for seismo-acoustic conversion validates this physical process, and demonstrates the low sensitivity of both microphones and barometers to ground accelerations. A second infrasonic pulse is observed 0.5 s after the shot. It is attributed to the infrasounds produced by the strong ground movement just above the buried seismic source because their propagation speed from the source to the receiver (about 380 m s^{-1}) correspond the one of acoustic waves.

3.3 Constraints on the incidence angle of the infrasonic waves from antenna processing of the infrasound instruments

Fig. 5(b) shows a time–altitude plot of the infrasound instruments deployed on the ground and below the balloon. Two arrivals are clearly detected whereas a very first one is close to noise level. The first two pulses propagate upward with vertical velocity of about 356 m s^{-1}, close to estimated sound speed (345 m s^{-1}), which suggest an almost vertical incidence indicating that these infrasonic waves are created just below the balloon. Examination of the multi-instrumental ground recordings (Fig. 4) shows that the second arrival correspond roughly to the one created by the surface wave ground motion, whereas the first one is due to the passing *P* wave. The latest arrival presents a vertical velocity much higher than sound speed, thus suggesting that these infrasounds arrive with a much higher incidence angle, presumably pointing in direction of the shot area. In addition, the 'M' waveform shape is very similar to the direct infrasound signals from underground explosions described by Jones *et al.* (2014) and Bowman (2019).

Antenna processing has been performed by using the two sensors deployed below the balloon for the two main infrasonic waves

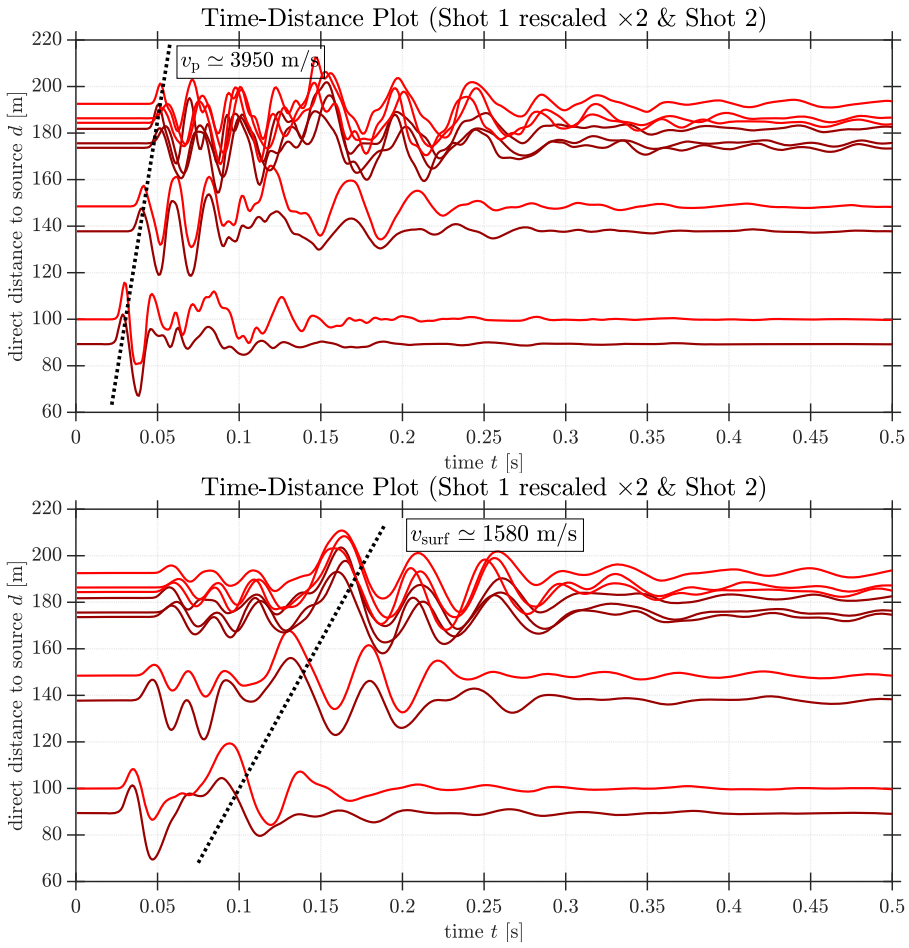

Figure 3. Time–distance plots of the vertical ground velocity normalized in amplitude. Data are bandpass filtered in the 0.5–1000 Hz range on top, and in the 0.5–20 Hz range at the bottom. The distance d is the direct distance to the explosive charges, in meters. v_p and v_{surf} stand, respectively, for P- and surface wave velocities.

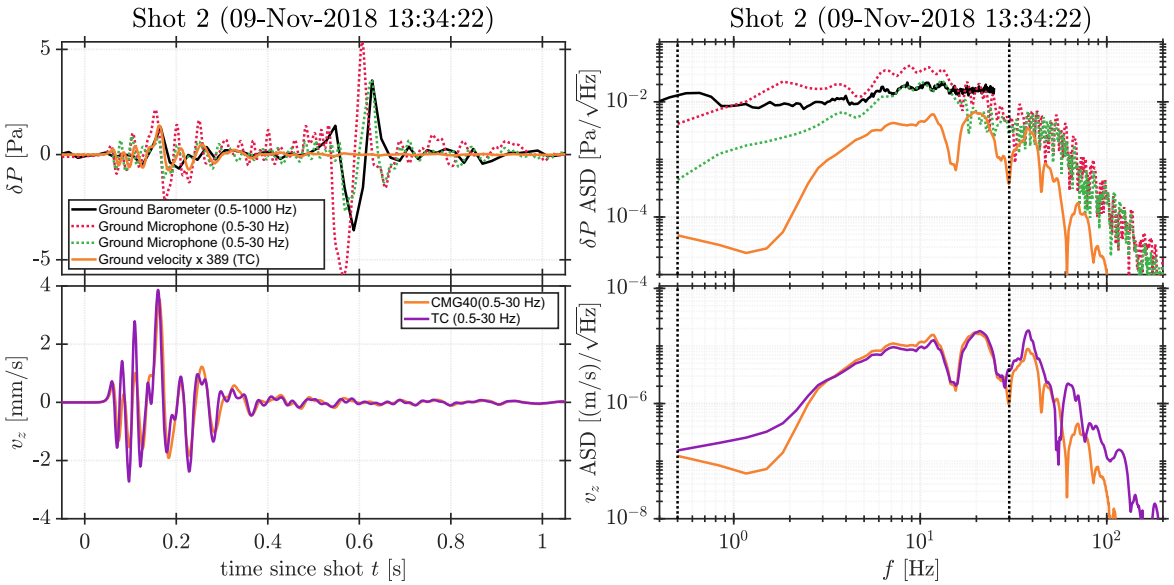

Figure 4. Comparison of collocated pressure perturbations (on top) and ground velocities (on the bottom) at 187 m horizontal distance from the second shot. On the left, signals in the time domain. On the right, amplitude spectral densities. Pressure data from the two microphones (red and green dashed lines), the infrasound sensor (black plain line) and theoretical acoustic prediction from ground velocities (gold plain line) are shown on top plots. Ground velocities from two close-by seismometers CMG40 (gold plain line) and TC120 (magenta plain line) are shown on bottom plots. All data are bandpass filtered in the 0.5–30 Hz range.

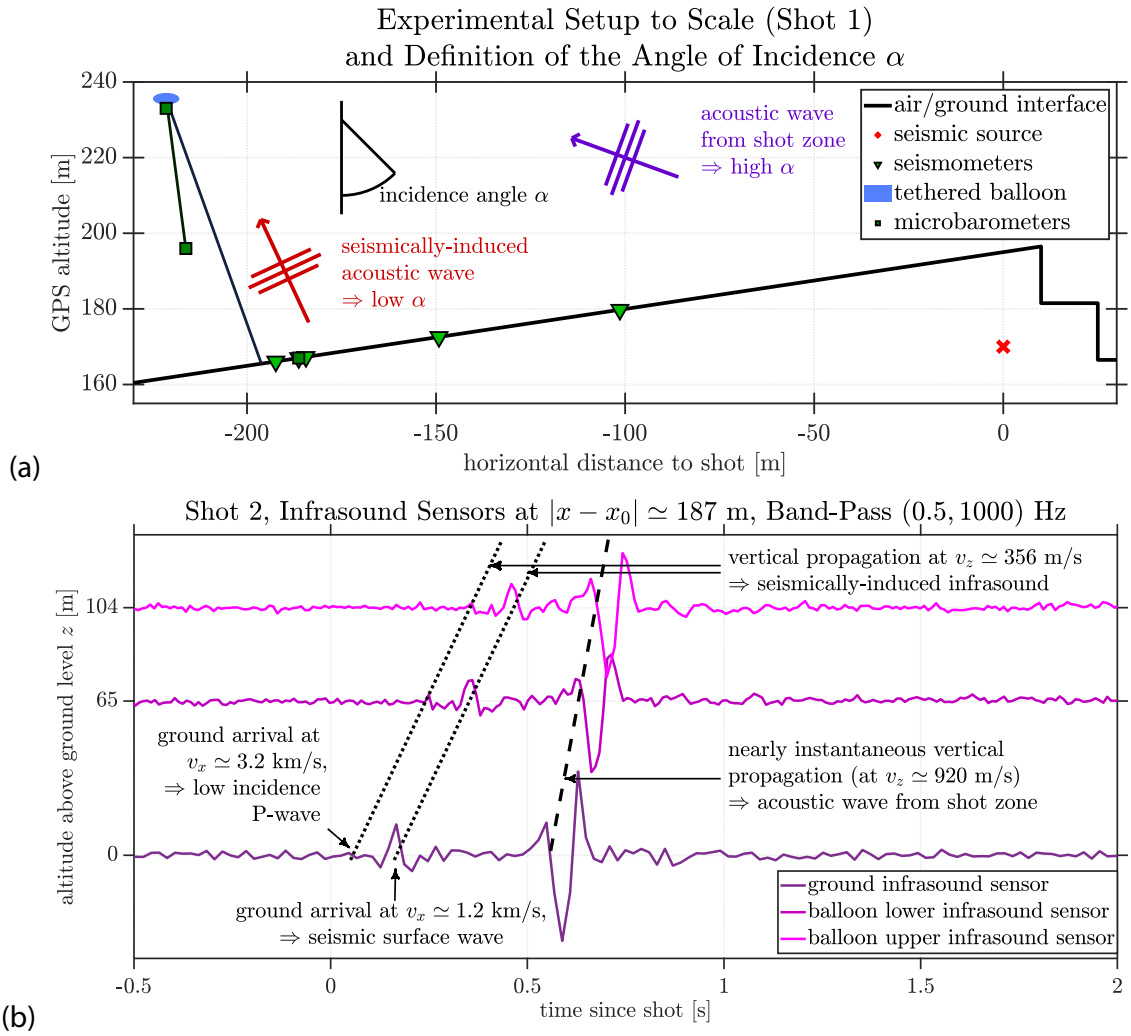

Figure 5. (a) Cross-section of the experimental setup for the first shot, and definition of the incidence angle α for airborne waves impinging the balloon. The positions of the ground instruments are exact (see Section 2.2). The positions of the airborne microbarometers were recovered using the GPS altitudes, the timings of the acoustic arrivals and the speed of sound deduced from temperature measurements (see Section 2.3). (b) Normalized pressure records from the three infrasound instruments, as a function of their altitude above ground level, for the second shot. Labels indicate our interpretation of the various arrivals.

(see Appendix A for a description of the geometry). Results are shown in Fig. 6 and Table 1. A simple correlation function of the waveforms and a conversion of time delays into incidence angles by using atmospheric sound speed allow to recover identical incidence angles of $17^\circ \pm 10^\circ$ for the first arrival for the two shots, whereas second arrival presents incidence angles of $81^\circ \pm 5^\circ$ for the first shot and $69^\circ \pm 5^\circ$ for the second shot. The low incidence angles obtained for the first arrival validate our interpretation as infrasonic waves created by seismic surface waves just below the balloon. The high incidence angles obtained for the second arrival validate our interpretation as infrasounds created by the strong ground movements above the shot zone. The smaller incidence angle obtained for the second shot relative to the first one is consistent with the fact that this second shot was closer to the instruments than the first one. The overall analysis validate the capability of such deployments to recover the arrival incidence of infrasonic waves with antenna processing methods. Moreover, it demonstrates that these deployments are able to discriminate infrasonic waves coming from below to the ones arriving at an almost horizontal incidence. Such computation was also performed successfully for the same set of airborne microbarometers on another experiment (Krishnamoorthy *et al.* 2019).

3.4 Constraints on the arrival direction of infrasonic waves from the accelerometers taped on the balloon envelope

The data from the IMU sensors deployed on the balloon envelope are processed to transfer these from IMU reference frame (RF) to balloon RF, and then to experiment RF by using magnetic field measurements internal to these sensors in order to know their azimuth relative to Earth's magnetic field. This last step is crucial to correct for balloon rotations and to ensure proper knowledge of balloon orientation during each shot. The data analysis presented in Fig. 7 exhibits the time-series of the accelerometers as well as their spectra. Infrasonic signals are recorded by the accelerometers in the 10–30 Hz frequency range during the shot, thus demonstrating their capability to detect the infrasounds from the balloon movements. Furthermore, it also shows that some modes of oscillations of the balloon-tether system are excited by the acoustic waves below 1 Hz. After the shot, a peak of frequency between

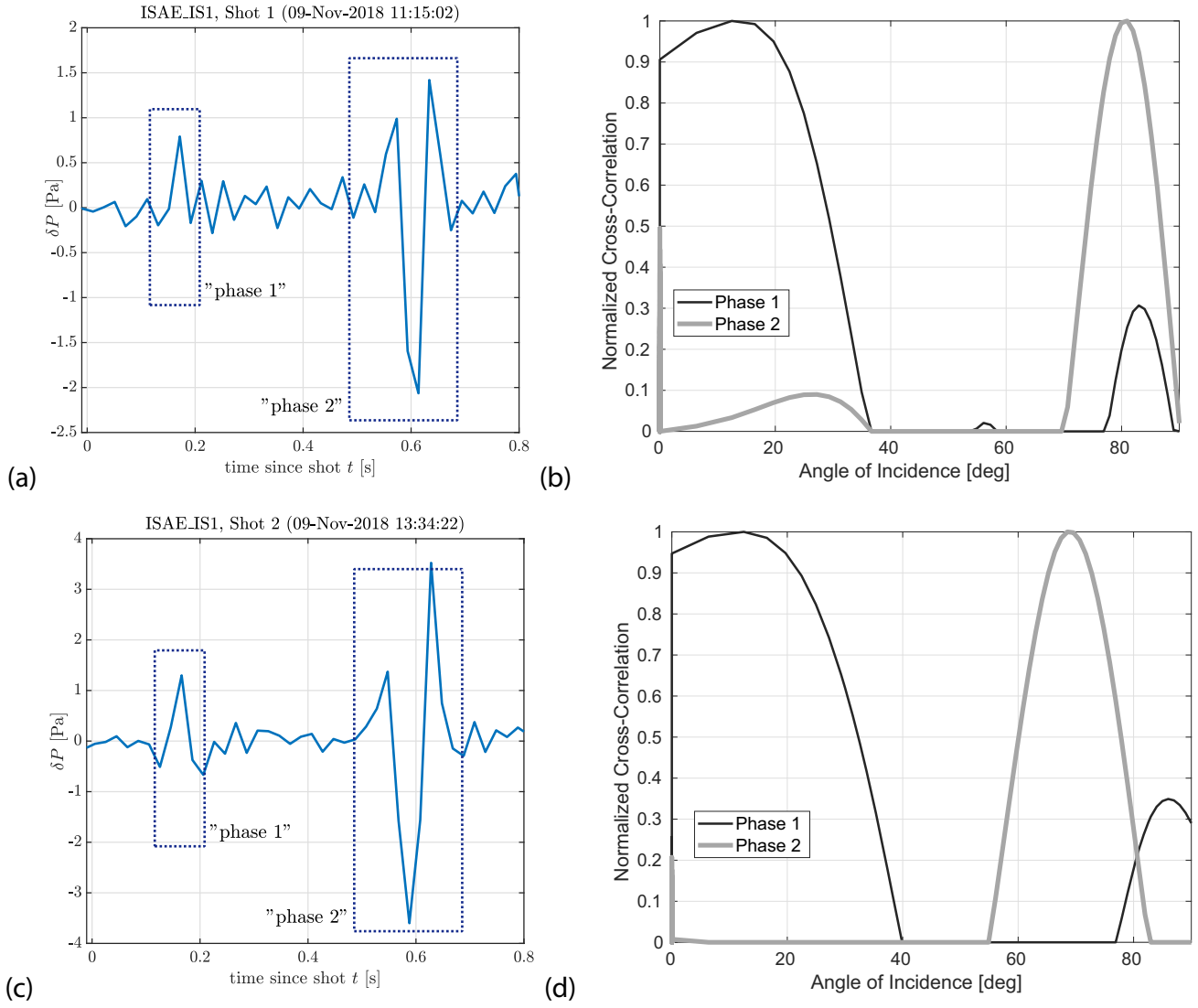

Figure 6. On the left (a) and (c): records of ground pressure variations just below the balloon and time window considered for the two main arrivals. On the right (b) and (d): correlation coefficients of the waveforms of the two main phases between the two infrasound sensors deployed below the balloon as a function of wave incidence angle (angle with respect to the vertical, in degrees). Records and incidence angle analysis are presented for the first shot, respectively the second shot, on the top (a) and (b), respectively on the bottom (c) and (d). The theoretical angles are computed geometrically for each phase in Appendix A.

Table 1. Angle of incidence (relative to vertical) of the two phases around shots 1 and 2, computed with antenna processing of barometers data and with IMUs data compared to theoretical values. α is the angle of incidence, measured with barometer antenna or IMUs (α_{exp}) and theoretical (α_{th}). Likewise, ϕ is the azimuth relative to shot direction, measured with barometer antenna or IMUs (ϕ_{exp}), and theoretical (ϕ_{th}). The theoretical angles are computed geometrically for each phase (Appendix A, eqs A4 and A8). The Δ values express the absolute values of the difference between theoretical and measured estimates of the parameters. The theoretical azimuth is zero the experiment reference frame. 'NA' is indicated for not applicable.

Sensor	Phase	α_{exp} (°)	α_{th} (°)	$\Delta\alpha$ (°)	ϕ_{exp} (°)	ϕ_{th} (°)	$\Delta\phi$ (°)
Barometer antenna	Seismically induced	17	21.2	4.2	NA	0	NA
	acoustic	81	72.9	8.1	NA	0	NA
Acc. sensor no. 5	Seismically induced	13.9	21.2	7.3	32.9	0	32.9
	acoustic	58.0	72.9	14.9	4.7	0	4.7
Acc. sensor no. 3	Seismically induced	23.4	21.2	2.2	−116.0	0	116.0
	acoustic	69.9	72.9	3	−28.1	0	28.1

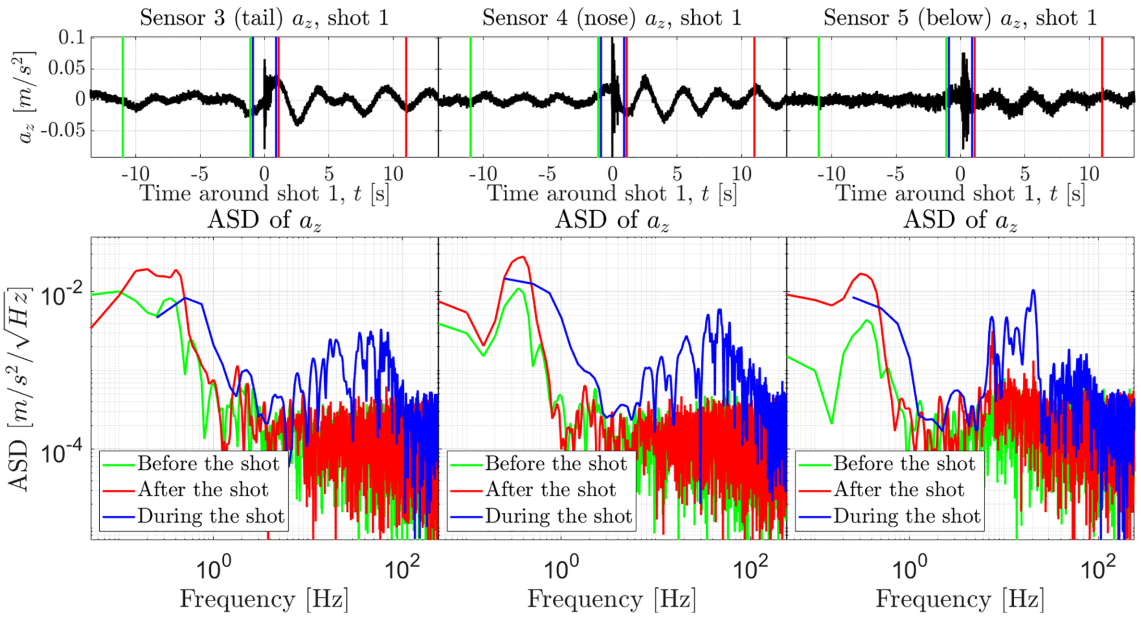

Figure 7. ASD of the vertical acceleration (de-trended) of the three sensors in the balloon referential, around shot 1. The ASD are plotted with different windows of time represented by the coloured lines. The ASD exhibit the tethered-balloon resonance modes below 1 Hz, as well as the infrasonic signals in the 10–30 Hz frequency range during the shot.

0.3 and 0.4 Hz seems to be preponderant. It is also present before the shot, but less preponderant. Lambert & Nahon (2003) simulated the stability analysis of a stream-lined tethered balloon. They showed that the resonant modes of the tethered balloon system are similar to the analytic reference frequencies for the motion of a buoyant mass on a string. The three principal modes are: the pendulum mode, the axial spring mode, and the tether's transverse mode. They are calculated with the parameters of the balloon used in the experiment. The axial spring mode derived is 0.39 Hz. The first and second tether's transverse are computed to be 0.33 and 0.66 Hz. These results corroborate the experimental observations on the acceleration spectral density (ASD) of the signals. Thus, the frequency content below 1 Hz of the acceleration data collected by the sensors could be explained by the modes of the tethered balloon system. We do not expect contamination by seismic waves through the tether because the balloon-tether system is acting as a low-pass filter cutting the high-frequency seismic forcing of the tether.

In order to retrieve the arrival direction of the seismic waves and to discriminate the different phases, the polarization of the accelerations induced by the waves is studied. Fig. 8 shows the polarization of the acceleration around shot 1 for the sensor at the tail of the balloon (no. 3) and the sensor below the balloon (no. 5). The sensor located at the nose of the balloon (no. 4) is not considered because of its strong sensitivity to oscillation modes and its complex pattern of acceleration during the shots, certainly induced by a complex combination of accelerations and rotations of the balloon. For the two sensors considered, the records clearly present two distinct arrivals, the second one having much more horizontal acceleration than the first one which has an almost vertical polarization. A principal component analysis (PCA) of the polarization of these two arrivals is performed. The incidence angles obtained are presented in Table 1. The incidence angles obtained are consistent with the ones measured for the infrasonic waves within 15°. However, the arrival azimuths (defined relative to shot direction) are consistent with shot direction only for the sensor taped at the bottom of the balloon (no. 5). The sensor at the tail of the balloon (no. 3) appears to be strongly contaminated by balloon rotations and deformations induced by the infrasonic waves and/or seismic waves acting on the tether.

4 VALIDATION USING FULL-WAVE NUMERICAL SIMULATIONS

4.1 Presentation of the simulation tool

A full-wave 2-D simulation reproducing the first shot was performed in order to validate the tool and confirm measured arrivals in data. The simulation tool, SPECFEM-DG, extends the widely used SPECFEM software that employs a spectral element method (Komatitsch & Vilotte 1998; Komatitsch & Tromp 1999; Tromp *et al.* 2008) to model seismic wave propagation. SPECFEM stands for SPECtral Finite Elements Method, and the DG extension stands for Discontinuous Galerkin. The main evolution introduced in SPECFEM-DG is the coupling to the full system of Navier–Stokes equations for atmospheric media, as detailed by Brissaud *et al.* (2017).

The computational domain D is 2-D, and is composed of a fluid domain D^{f} and a solid domain D^{s}, both separated by an interface Γ^{fs} where a mechanical coupling occurs. Said coupling is done in two directions. Fluid-to-solid coupling is done by enforcing continuity of the normal stress and of the normal velocity. Solid-to-fluid coupling is done following the method described by Terrana *et al.* (2018). Outer boundary conditions are chosen absorbing on all (left/right/bottom/top) boundaries.

The numerical method relies on weak formulations through a spectral element method, continuous for the elastic domain (Komatitsch & Vilotte 1998; Komatitsch & Tromp 1999; Tromp *et al.* 2008) and discontinuous for the fluid domain (Brissaud *et al.* 2017). Time integration is explicit (optimal five-step fourth-order Runge–Kutta scheme (Carpenter & Kennedy 1994)).

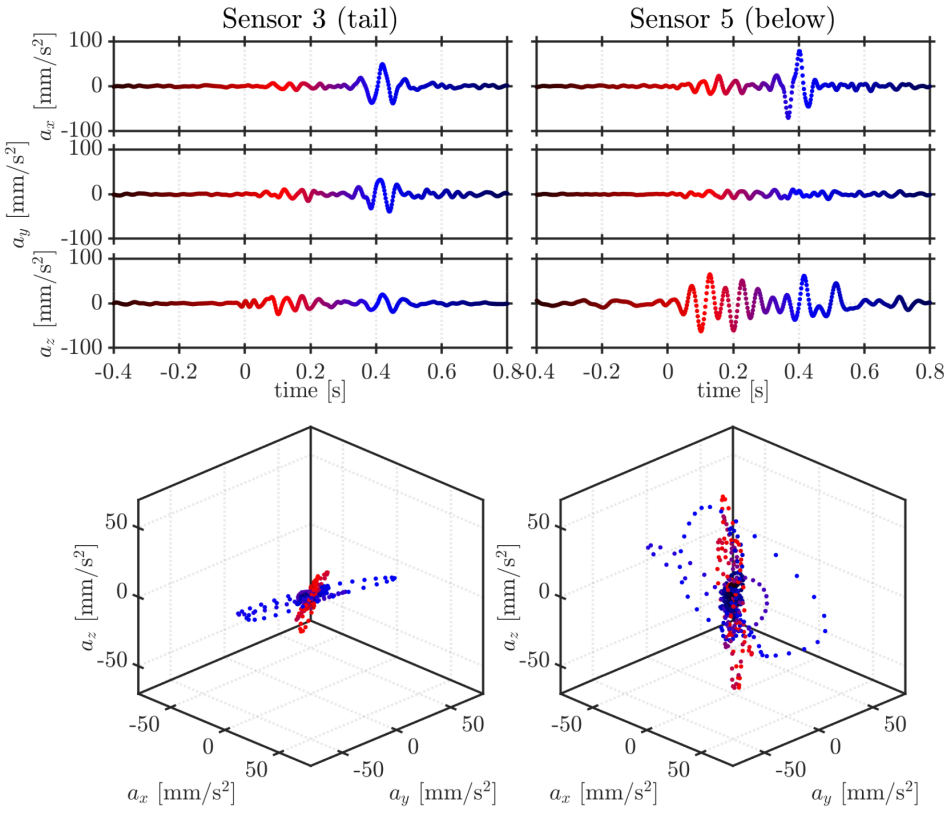

Figure 8. Polarization of the acceleration of sensor no. 3 (balloon tail, on the left) and sensor no. 5 (below balloon, on the right) around shot 1. Top: acceleration records of the sensors. Bottom: 3-D view of the accelerations over time. The data are filtered with a fourth-order bandpass filter in the 5–30 Hz range. The colour of each point is defined by its acquisition time around the shot (see top panel). The reference time is the time of the first vertical acceleration perturbation due to the shot.

SPECFEM-DG can intrinsically model waves in all frequency bands (Brissaud *et al.* 2017; Spiga *et al.* 2018), and especially in the 1–100 Hz range of interest here. The mechanical coupling enables the conversion of seismic waves into atmospheric acoustic waves (Brissaud *et al.* 2017; Martire *et al.* 2018). The outputs of this software are full wavefields. Consequently one can extract, in particular, simulated seismograms (of, e.g. velocities $V_{x,z}(t)$ or accelerations $A_{x,z}(t)$) and simulated absolute pressure records (including pressure perturbations $\Delta P(t)$).

4.2 Computational domain and receivers

The simulation is performed in a 2-D vertical plane along azimuth 82.83°, that is, along the seismic line (Section 2.2), as seen from the South (see Fig. 5a).

The ground/atmosphere boundary Γ^{fs} follows the topography of the experiment location, which was acquired by GPS measurements. The origin of the simulation's RF is chosen at the surface above the borehole for the first shot, such that the explosive charge lies at $[x, z] = [0, -25]$. We define the z-axis as pointing upwards, and the x-axis pointing to the West (note that the x-axis points in the opposite direction for the measurements ' RF).

The complete numerical domain D spans from a maximum depth of 250 m to a maximum altitude of 250 m. The horizontal span of the computational domain is chosen to include the cliffs to the East and the field to the West, and thus spans a total of 500 m.

Recording stations are spread along the interface, sampling either ground pressure perturbations ΔP or ground velocity $V_{x,z}$. We also add stations to model the instruments sensors carried by the balloon: infrasound sensors (pressure perturbations ΔP) and IMUs (acceleration $A_{x,z}$).

4.3 Ground and atmospheric models

The atmospheric model is chosen isothermal, without wind, and range-independent. In order to conserve hydrostatic equilibrium, the ambient pressure P is chosen such that $\overrightarrow{\nabla} P = \rho \overrightarrow{g}$ (with ρ the ambient density and $\overrightarrow{g} := g\overrightarrow{e_z}$ the local gravity). Atmospheric intrinsic attenuation was neglected: both the dynamic viscosity μ and the thermal conductivity κ were set to zero. These conditions are close to the experimental ones due to the small size of the experiment. The following equation system eq. (1) describes the initial conditions of the atmospheric model:

$$\forall \overrightarrow{x} := [x, z] \in D^{\mathrm{f}}, \quad \begin{cases} \rho\left(\overrightarrow{x}\right) &= \rho_0 e^{-z/H}, \\ P\left(\overrightarrow{x}\right) &= \rho\left(\overrightarrow{x}\right) gH, \\ \overrightarrow{v}\left(\overrightarrow{x}\right) &= \overrightarrow{0}, \\ \mu\left(\overrightarrow{x}\right) &= 0, \\ \kappa\left(\overrightarrow{x}\right) &= 0, \end{cases} \tag{1}$$

with D^{f} the fluid part of the computational domain, ρ the ambient density, P the ambient pressure, $\overrightarrow{v}$ wind, μ the dynamic viscosity

and κ the thermal conductivity. The values are:

$$\begin{cases} c_{0,\mathrm{exp}} = & 345.13 & \mathrm{m\,s^{-1}}, \\ P_{0,\mathrm{exp}} = & 99399 & \mathrm{Pa}, \\ g = & 9.80665 & \mathrm{m\,s^{-2}}, \\ \gamma = & 1.401, & \\ H = \frac{c_{0,\mathrm{exp}}^2}{\gamma g} & = 8670 & \mathrm{m}, \\ \rho_0 = \frac{\gamma P_{0,\mathrm{exp}}}{c_{0,\mathrm{exp}}^2} & = 1.1691 & \mathrm{kg\,m^{-3}}, \end{cases} \tag{2}$$

where $c_{0,\,\mathrm{exp}}$ is the experimental speed of sound (see Section 2.3), $P_{0,\,\mathrm{exp}}$ is the experimental ambient pressure (measured by the ground infrasound sensor), g is Earth's gravity, γ is the adiabatic ratio, H is the scale height of the atmosphere computed using the perfect gas hypothesis (PGH), and ρ_0 is the surface density computed using the PGH.

For the ground model, a single limestone deposit was considered according to quarry specifications and our active seismic investigation (Section 3.1). The elastic parameters are chosen as follows: $v_\mathrm{p} = 4000\ \mathrm{m\,s^{-1}}$ and $v_\mathrm{s} = 1720\ \mathrm{m\,s^{-1}}$, respectively for the *P*- and *S*-wave velocities (Section 3.1), $\rho^\mathrm{s} = 2550\ \mathrm{kg\,m^{-3}}$ for the density (Bourbié *et al.* 1987, table 5.2), and $Q_\mathrm{p} = 14.9$ and $Q_\mathrm{s} = 12.1$ respectively for the *P*- and *S*-wave quality factors (Toksöz *et al.* 1979,table 1).

4.4 Source

The source is modelled as an isotropic moment rate tensor:

$$\overline{\overline{M}}\left(t, \overrightarrow{x}\right) = A e^{-(\pi f_0 t)^2} \delta_{\overrightarrow{x_0}}\left(\overrightarrow{x}\right) \begin{bmatrix} 1 & 0 \\ 0 & 1 \end{bmatrix}, \tag{3}$$

where $A = 7.416 \times 10^9$ is an amplification factor, $f_0 = 40$ Hz is the dominant frequency, δ is the Dirac function (the source is applied at a single point in space) and $\overrightarrow{x_0} = [0, -25]$ m is the source localization in $[x, z]$ coordinates. The depth of the source is chosen according to the buried explosions' setup (Section 2.2). The dominant frequency is set according to the peak frequency observed on the seismometers (Fig. 4). The amplification factor A was chosen such that the seismic moment corresponds to $\int_{-\infty}^{\infty} M\left(t, \overrightarrow{x} = \overrightarrow{x_0}\right)\ \mathrm{d}t = 1.046 \times 10^8$ J =25 kg TNT-equivalent.

4.5 Simulations' results

Fig. 9 is a snapshot of the simulation, showing the various acoustic and seismic wave fronts propagating in the numerical domain. The seismic surface wave is clearly visible in the solid domain with vertical velocity wave fronts. The head waves created by the seismic *P* and surface waves appear in the atmosphere as almost horizontal wave fronts. The acoustic waves created by the ground uplift at the source are propagating as circular wave fronts centred on the source location. Acoustic waves diffracted by the topography (cliffs) are also visible.

4.5.1 Ground velocity and atmospheric pressure perturbations

The simulation outputs are compared to the real pressure and ground motion data in Fig. 10. The arrival times, amplitudes and waveforms of *P* and surface waves are properly reproduced for seismic sensors. However, the *P* wave presents lower frequencies in the synthetics than in the data. The coda of seismic waves cannot be reproduced with such a simple model. Due to higher energy at low frequencies for the *P* wave, the associated infrasounds in the atmosphere are over estimated in the frequency range of barometer sensors (below 20 Hz). However, the infrasound generated by the seismic surface waves have the proper amplitude. The predictions of the arrival times of the various infrasounds suffers from uncertainties on the positions of the barometers tethered to the balloon and from approximations in the overall geometry of the experiment. These discrepancies are particularly visible for the last infrasound wave train due to ground uplift just above the explosive source. Because these waves propagate at speed of sound, the errors on the sensor positions generate large errors on the arrival times of infrasonic waves. The amplitude of infrasonic waves coming from the shot zone are underestimated by a factor 4–5. This discrepancy can possibly be explained by combined effects due to the lack of confinement of the explosives which is generating a strong venting in the source region (Bowman *et al.* 2014), and the lack of representativeness of 2-D spall simulations. Another potential source of discrepancy is ascribed to local 3-D variations of ground uplift and topography close to the explosive source. Despite these discrepancies, the simulation tool is able to predict the overall seismic and infrasonic wave amplitudes and arrival times with a realistic source scaling.

4.5.2 Inertial measurements

Fig. 11 compares the accelerometer data recorded on the balloon envelope to the corresponding synthetics. On synthetics, one can clearly identify the three phases of interest: the infrasound induced by the seismic *P* wave, the infrasound induced by the seismic surface wave, and the acoustic wave from the shot zone. These three phases can easily be associated with corresponding features in accelerometer data.

We remark that all synthetics over-estimate data by a factor $\simeq 40$, although arrival times closely match. We ascribe this amplitude discrepancy to the fact that we do not model the balloon's inertia. The real accelerometers measure the motion of the balloon envelope, whereas our simulated accelerometers record air motion. The signal polarization, and the relative amplitudes and waveforms along the horizontal direction are properly reproduced. Whereas the data along the vertical component present more complexity, probably due to the response of the balloon/tether system. The wave packet of the seismic surface waves observed in Fig. 10, are quite well transmitted, in duration and shape, to balloon accelerations for both data and synthetics. However, these results call for a more complete analysis of the mechanical coupling between the balloon envelope and the surrounding air.

5 CONCLUSIONS

The active seismic source experiment presented in this study demonstrates the capability of balloon platforms to record the infrasonic waves created by the seismic waves. Infrasonic waves created by both seismic waves below the balloon and strong ground motions above the explosive sources are detected and clearly separated. Moreover, both antenna processing of infrasound instruments deployed below the balloon and polarization analysis of accelerometers taped on the balloon envelope allows to discriminate between infrasonic waves propagating at low and high incidence angles. Antenna processing of two infrasound sensors separated by a vertical distance of 40 m allows to recover the incidence angle of infrasounds with an uncertainty between 5° and 10°. For the polarization analysis of the accelerometer records, their response strongly depends on the sensor location in the tethered balloon system due to

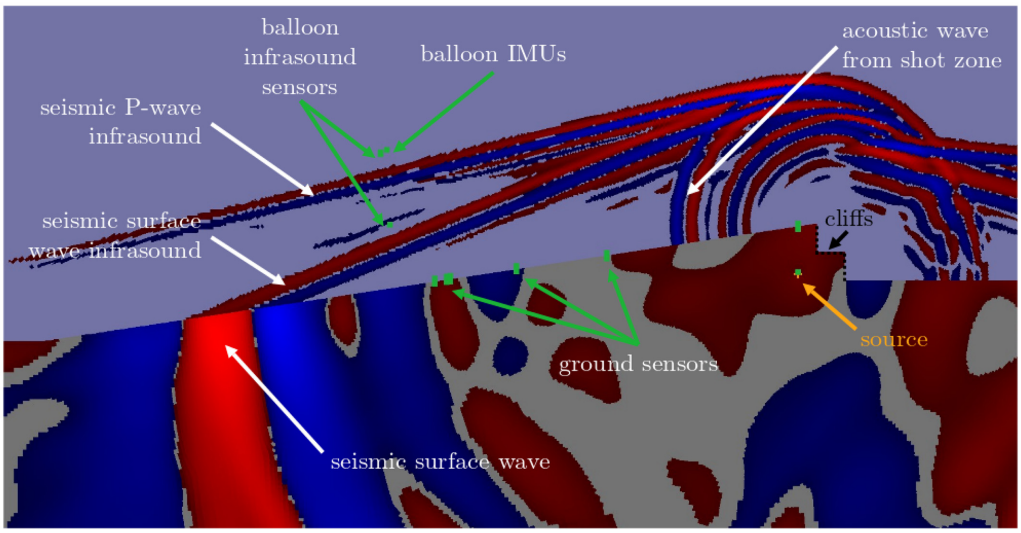

Figure 9. Snapshot of the full-wave simulation discussed in Section 4, at $t = 0.250$ s. Colours encode the sign of the signals, red meaning positive and blue negative, using a saturated colour bar (maximum of the colour bar at ± 1 per cent of maximum amplitude in either the fluid or the solid domain); this saturation allows to visualize signals of very different amplitudes. The discussion of amplitudes is reported to Fig. 10. The dark grey background is the solid domain D^{s}, whereas the purple background is the fluid domain D^{f}; remark the topography Γ^{fs} separating the two domains. In D^{s} the vertical velocity field V_z is represented, whereas the colours encode the pressure perturbations' field ΔP in D^{f}. The yellow cross shows the source location. The green dots represent recording stations; airborne recording stations represent either the balloon-borne infrasound sensors or the IMUs on the balloon en envelope; however note that the balloon itself is not modelled. Arrows pinpoint interesting features.

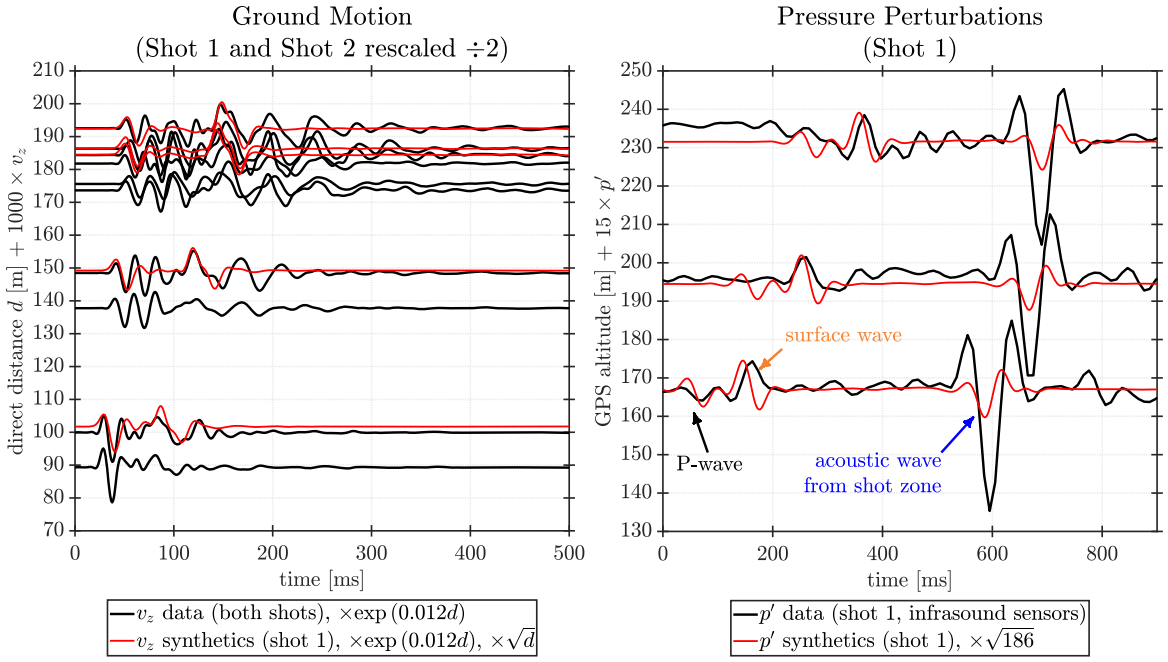

Figure 10. Comparison between record sections of the data (black) and corresponding synthetics (red). Left: vertical ground velocity along the seismic line, as a function of direct distance to the source. Data for both shots and synthetics from the simulation of shot 1 are presented. Right: pressure perturbations as a function of GPS altitude. Data and synthetics for shot 1 are presented (with the airborne infrasound sensors located as in Fig. 5.a). All quantities related to shot 2 (data or synthetics) are scaled up by a factor $\frac{1}{2}$ due to the NEM being 50 kg for shot 2 instead of 25 kg for shot 1. In order to take into account the instrument response of seismometers and barometers, all data and synthetics are filtered with a fourth-order low-pass filter, with cut-off 100 Hz for the left-hand panel (see ground motion spectra in Fig. 4, bottom right panel) and 20 Hz for the right-hand panel (see infrasound spectra in Fig. 4, top right panel). On left-hand panel, for the sake of readability, all amplitudes were scaled by a common distance-dependent factor $e^{0.012d}$ in order to compensate for the seismic attenuation with distance. On both panels, synthetics were scaled by a $\sqrt{d}$ factor to account for the difference in geometrical spreading between 2-D (simulations) and 3-D (data). On the right-hand plot, $d = 186$ m corresponds to position of the ground infrasound sensor.

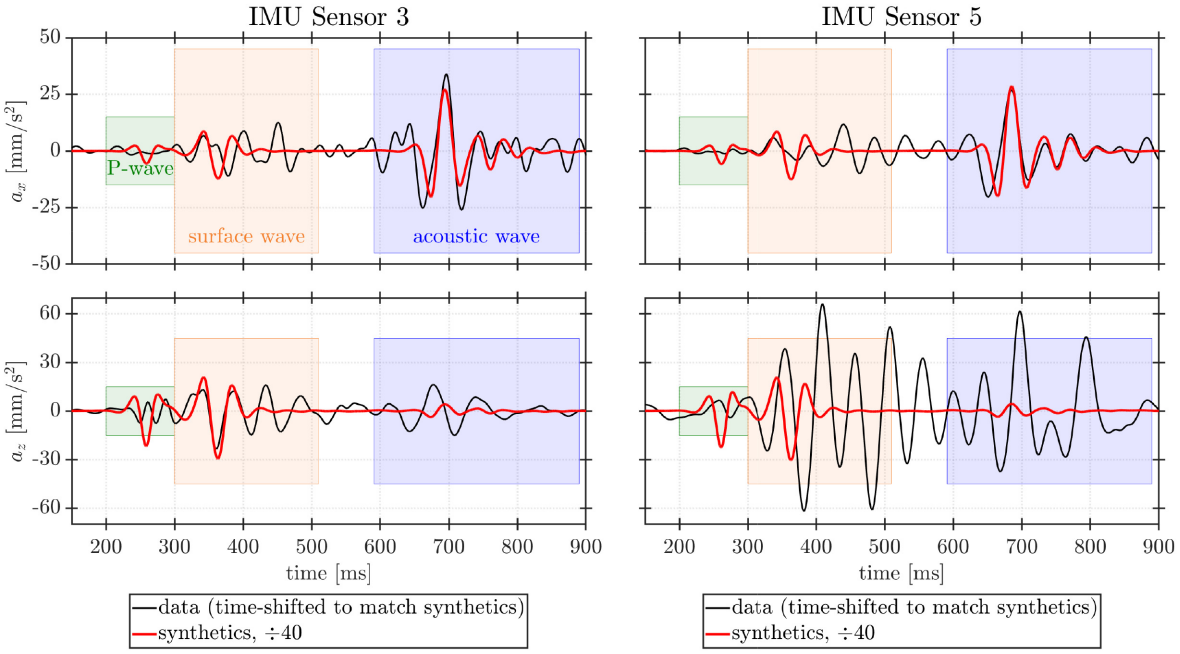

Figure 11. Comparison between accelerometer data (black, see also Fig. 8) and corresponding synthetics (red) for the first shot. Left: IMU no. 3 (balloon tail). Right: IMU no. 5 (below balloon). Both data and synthetics are filtered with a fourth-order bandpass in the 4.5–30 Hz range (see IMU spectra in Fig. 7). Since the IMUs' time reference could not be constrained, IMU data were time-shifted to match synthetic arrivals. Synthetic amplitudes were downscaled; see explanation in Section 4.5.2. Coloured sections indicate our interpretation of the various arrivals. The green section corresponds to the infrasound induced by the seismic *P* wave; although clear in synthetics, it is below noise level for the IMU data. The orange section corresponds to the infrasound induced by the seismic surface wave (see also the red points in Fig. 8). The blue section corresponds to the acoustic wave from the shot zone (see also the blue points in Fig. 8), which is underestimated in synthetics (see Fig. 10).

balloon rotations and deformations. However, the uncertainty on incidence angle is around 20°. The accelerometers sensors located as close as possible to the balloon centre of gravity and/or to the centre of forces exerted by the tether appears less sensitive to balloon rotations and deformations induced by the infrasonic waves. This experiment also validates both the simple physics of seismo-acoustic coupling and our 2-D full-wave numerical simulation tool.

For terrestrial active source experiments, the deployment of infrasound sensors on the ground and on tethered balloons would allow to better constrain the acoustic signals contaminating the seismic records, the source characteristics (Bowman 2019) and the presence of soft subsurface layers (Martire *et al.* 2018). This experiment is a clear terrestrial demonstrator of the concept of Venus balloon platforms for atmospheric seismology. It quantifies the capabilities of various instruments to discriminate between different infrasonic sources based on their incidence angle. Despite differences in frequency content, wavelengths and balloon system (tethered instead of freeflying), our study demonstrates the interest of both infrasound instrument antennas and accelerometers attached to balloon envelope for such measurements. Our results also suggest that, for Venus case, a careful study of the oscillation/deformation modes of the balloon-infrasound antenna system must be performed to ensure that these signals are not contaminating the frequency range of interest. An application of these methods in Venus atmosphere also requires additional measurements such as air temperature and composition in order to estimate sound speed, balloon orientation to estimate the arrival azimuth, and balloon motions to correct the associated pressure variations.

Despite the advances performed in a such a controlled environment, some observations of the acoustic waves generated by quakes on a freeflying balloon platform, in the low atmosphere or the stratosphere, are still required to fully validate the science case of atmospheric seismology with Venus balloon platforms. Such observations would be much more realistic in terms of seismic source, observation environment and observation geometry.

ACKNOWLEDGEMENTS

For the support they provided, the authors thank Fabrice Martin and Romain Redonnet from the COLAS company, as well as Bruno Chaput and Guillaume Passavy from the Titanobel company. The authors thank the TGCC (Paris, France, project GENCI gen10476) and CALMIP (Toulouse, France, project no. p1404) computing centres for HPC ressources. The authors thank both the 'Direction Générale de l'Armemen' (French DOD) and the 'Région Occitanie' for funding the PhD grant of Léo Martire. This study was supported by CNES research projects. The data set presented in this study is available at the following Zenodo repository: https://doi.org/10.5281/zenodo.4067121 The authors acknowledge Florian Fuchs and an anonymous reviewer for their constructive remarks that allowed to improve this study.

REFERENCES

Arrowsmith, S.J., Burlacu, R., Pankow, K., Stump, B., Stead, R., Whitaker, R.W. & Hayward, C., 2012. A seismoacoustic study of the 2011 January 3 Circleville earthquake, *Geophys. J. Int.*, **189**(2), 1148–1158.

Averbuch, G., Waxler, R.M., Smets, P. S.M. & Evers, L.G., 2020. Probabilistic inversion for submerged source depth and strength from infrasound observations, *J. acoust. Soc. Am.*, **147**(2), 1066–1077.

Banister, J.R. & Hereford, W.V., 1982. Rummy high-altitude pressure measurements and analysis, Tech. Rep., Sandia National Laboratories, Albuquerque, NM 87185, USA.

Banister, J.R. & Hereford, W.V., 1991. Observed high-altitude pressure waves from an underground and a surface explosion, *J. geophys. Res.,* **96**(90), 5185–5193.

Bourbié, T., Coussy, O. & Zinszner, B., 1987. *Acoustics of Porous Media,* Editions Technip, Paris.

Bowman, D.C., 2019. Yield and emplacement depth effects on acoustic signals from buried explosions in hard rock, *Bull. seism. Soc. Am.,* 10.1785/0120180285.

Bowman, D.C. & Lees, J.M., 2017. A comparison of the ocean Microbarom recorded on the ground and in the stratosphere, *J. geophys. Res.: Atmos.,* **122**(18), 9773–9782.

Bowman, D.C. & Lees, J.M., 2019. Data from: upper atmosphere heating from ocean-generated acoustic wave energy, 10.1029/2018GL077737.

Bowman, D.C., Taddeucci, J., Kim, K., Anderson, J.F., Lees, J.M., Graettinger, A.H., Sonder, I. & Valentine, G.A., 2014. The acoustic signatures of ground acceleration, gas expansion, and spall fallback in experimental volcanic explosions, *Geophys. Res. Lett.,* **41**(6), 1916–1922.

Bowman, D.C., Lees, J.M., Cutts, J.A., Komjathy, A., Young, E.F., Seiffert, K., Boslough, M. & Arrowsmith, S.J., 2018. Geoacoustic observations on drifting balloon-borne sensors, in *Infrasound Monitoring for Atmospheric Studies,* pp. 125–171, Springer International Publishing, Cham.

Brissaud, Q., 2017. *Modélisation numérique des ondes atmosphériques issues des couplages solide/océan/atmosphère et applications,* PhD thesis, Université Toulouse 3 Paul Sabatier.

Brissaud, Q., Martin, R., Garcia, R.F. & Komatitsch, D., 2017. Hybrid Galerkin numerical modelling of elastodynamics and compressible Navier-Stokes couplings: applications to seismo-gravito acoustic waves, *Geophys. J. Int.,* **210**(2), 1047–1069.

Carpenter, M.H. & Kennedy, C.A., 1994. Fourth-order 2N-storage Runge-Kutta schemes, *Nasa Tech. Memorand.,* **109112,** 1–26.

Didion, A. *et al.*, 2018. Remote sensing of venusian seismic activity with a small spacecraft, the vamos mission concept, in 2018 IEEE Aerospace Conference, AERO 2018, pp. 1–14, IEEE Computer Society, Conference date: 03-03-2018 Through 10-03-2018, 10.1109/AERO.2018.8396447.

Garcia, R.F., Lognonné, P.H. & Bonnin, X., 2005. Detecting atmospheric perturbations produced by Venus quakes, *Geophys. Res. Lett.,* **32**(16), 1–4.

Garcia, R.F., Drossart, P., Piccioni, G., López-Valverde, M. & Occhipinti, G., 2009. Gravity waves in the upper atmosphere of Venus revealed by CO_2 nonlocal thermodynamic equilibrium emissions, *J. geophys. Res. (Planets),* **114,** E00B32, doi: 10.1029/2008JE003073.

Hines, C.O., 1960. Internal atmospheric gravity waves at ionospheric heights, *Can. J. Phys.,* **38**(11), 1441–1481.

Jones, K.R., Whitaker, R.W. & Arrowsmith, S.J., 2014. Modelling infrasound signal generation from two underground explosions at the source physics experiment using the rayleigh integral, *Geophys. J. Int.,* **200**(2), 779–790.

Kherani, E.A., Lognonné, P., Kamath, N., Crespon, F. & Garcia, R., 2009. Response of the ionosphere to the seismic trigerred acoustic waves: electron density and electromagnetic fluctuations, *Geophys. J. Int.,* **176**(1), 1–13.

Komatitsch, D. & Tromp, J., 1999. Introduction to the spectral element method for three-dimensional seismic wave propagation, *Geophys. J. Int.,* **139,** 806–822.

Komatitsch, D. & Vilotte, J.-P., 1998. The spectral element method : an efficient tool to simulate the seismic response of 2D and 3D geological structures, *Bull. seism. Soc. Am.,* **88**(2), 368–392.

Krishnamoorthy, S. *et al.*, 2018. Detection of artificially generated seismic signals using balloon-borne infrasound sensors, *Geophys. Res. Lett.,* doi: 10.1002/2018GL077481.

Krishnamoorthy, S. *et al.*, 2019. Aerial seismology using balloon-based barometers, *IEEE Trans. Geosci. Remote Sens.,* 1–11, 10.1109/TGRS.2019.2931831.

Krishnamoorthy, S., Bowman, D.C., Komjathy, A., Pauken, M.T. & Cutts, J.A., 2020. Origin and mitigation of wind noise on balloon-borne infrasound microbarometers, *J. acoust. Soc. Am.,* **148**(4), 2361–2370.

Lambert, C. & Nahon, M., 2003. Stability analysis of a tethered aerostat, *J. Aircraft,* **40,** 705–715.

Lognonné, P., 2009. *Seismic Waves from Atmospheric Sources and Atmospheric/Ionospheric Signatures of Seismic Waves,* pp. 281–304, Springer Netherlands.

Lognonné, P., Clévédé, E. & Kanamori, H., 1998. Computation of seismograms and atmospheric oscillations by normal-mode summation for a spherical earth model with realistic atmosphere, *Geophys. J. Int.,* **135**(2), 388–406.

Lognonné, P.H. & Johnson, C.L., 2007. Planetary seismology, in *Treatise on Geophysics,* pp. 69–122, Tilman Spohn.

Lognonné, P.H., Karakostas, F., Rolland, L.M. & Nishikawa, Y., 2016. Modeling of atmospheric-coupled Rayleigh waves on planets with atmosphere: from Earth observation to Mars and Venus perspectives, *J. acoust. Soc. Am.,* **140**(2), 1447–1468.

Martire, L. *et al.*, 2018. Numerical simulation of the atmospheric signature of artificial and natural seismic events, *Geophys. Res. Lett.,* **45**(21), 085–12, doi: 10.1029/2018GL080485.

Pichon, A.L., 2005. Infrasound monitoring of volcanoes to probe high-altitude winds, *J. geophys. Res.,* **110**(D13), doi: 10.1029/2004JD005587.

Poler, G., Garcia, R.F., Bowman, D.C. & Martire, L., 2020. Infrasound and gravity waves over the Andes observed by a pressure sensor on board a stratospheric balloon, *J. geophys. Res.: Atmos,* doi: 10.1029/2019JD031565.

Sabatini, R., Snively, J.B., Bailly, C., Hickey, M.P. & Garrison, J.L., 2019. Numerical modeling of the propagation of infrasonic acoustic waves through the turbulent field generated by the breaking of mountain gravity waves, *Geophys. Res. Lett.,* **46**(10), 5526–5534.

Spiga, A. *et al.*, 2018. Atmospheric science with insight, *Space Sci. Rev.,* **214**(7), 109, doi: 10.1007/s11214-018-0543-0.

Stevenson, D., Cutts, J.A. & Mimoun, D., 2015. Probing the interior structure of Venus, Tech. Rep., Keck Institute for Space Studies, Pasadena, CA 91106, USA.

Sylvander, M., Ponsolles, C., Benahmed, S. & Fels, J.-F., 2007. Seismoacoustic recordings of small earthquakes in the Pyrenees: experimental results, *Bull. seism. Soc. Am.,* **97**(1 B), 294–304.

Terrana, S., Vilotte, J.-P. & Guillot, L., 2018. A spectral hybridizable discontinuous Galerkin method for elastic-acoustic wave propagation, *Geophys. J. Int.,* **213**(1), 574–602.

Toksöz, M.N., Johnston, D.H. & Timur, A., 1979. Attenuation of seismic waves in dry and saturated rocks: I. Laboratory measurements, *Geophysics,* **44**(4), 681–690.

Tromp, J., Komatitsch, D. & Liu, Q., 2008. Spectral-element and adjoint methods in seismology, *Commun. Comput. Phys.,* **3**(1), 1–32.

Young, E.F., Bowman, D.C., Lees, J.M., Klein, V., Arrowsmith, S.J. & Ballard, C., 2018. Explosion-generated infrasound recorded on ground and airborne microbarometers at regional distances, *Seismol. Res. Lett.,* **89**(4), 1497–1506.

Zettergren, M.D. & Snively, J.B., 2015. Ionospheric response to infrasonic-acoustic waves generated by natural hazard events, *J. geophys. Res.: Space Phys.,* **120**(9), 8002–8024.

Zettergren, M.D., Snively, J.B., Komjathy, A. & Verkhoglyadova, O.P., 2017. Nonlinear ionospheric responses to large-amplitude infrasonic-acoustic waves generated by undersea earthquakes, *J. geophys. Res. (Space Phys.),* **122**(2), 2272–2291.

SUPPORTING INFORMATION

Supplementary data are available at *GJI* online.

movie.gif

Please note: Oxford University Press is not responsible for the content or functionality of any supporting materials supplied by the authors. Any queries (other than missing material) should be directed to the corresponding author for the paper.

APPENDIX A: GEOMETRIC DETERMINATION OF THEORETICAL INCIDENCE ANGLES

First, the field where the seismometer line was deployed can be considered completely flat. The GPS altitude at the surface of the bore hole is $z_{\rm bh} = 195$ m ASL. The GPS altitude of the balloon's anchor is $z_{\rm ba} = 167$ m ASL. The balloon's anchor is situated at a surface range of $x_{\rm ba} = 187$ m from the bore hole. Consequently, the field is inclined, from true horizontal, at an angle:

$$\alpha_{\rm field} = \arcsin\left(\frac{z_{\rm bh} - z_{\rm ba}}{x_{\rm ba}}\right) = 8.611^\circ. \tag{A1}$$

Secondly, because of the difference in propagation speeds, acoustic waves induced by seismic surface waves are launched from the ground surface at an incidence of:

$$i_{\rm sa} = \arcsin\left(\frac{c}{v_{\rm surf}}\right), \tag{A2}$$

where $v_{\rm surf}$ is the surface wave speed and c is the atmospheric speed of sound. From seismic investigation (Section 3.1), we estimated $v_{\rm surf} = 1580 \pm 300$ m s^{-1}. From the PGH and temperature measurements, $c = \sqrt{\gamma R T_{0,\rm exp}/M_{\rm air}} \simeq 345.12$ m s^{-1}; where $\gamma = 1.401$ is the adiabatic ratio, R is the gas constant, $T_{0,\,\rm exp} = 21.9\,^\circ$C is the measured temperature at ground level during the first shot (see Section 2.3) and $M_{\rm air} = 0.028858$ kg mol^{-1} is the molar mass of dry air. Consequently,

$$i_{\rm sa} = 12.62^\circ. \tag{A3}$$

Since the infrasound sensors carried by the balloon are assumed to hang freely and thus almost vertically, they are expected to see an angle of arrival being the sum of the inclination of the terrain and of the seismo-acoustic signal launch angle. That is, using eqs (A1) and (A3):

$$\alpha_{\rm th,sa} = \alpha_{\rm field} + i_{\rm sa} \simeq 21.23^\circ. \tag{A4}$$

Now take the orthogonal projection of position of the infrasound sensors onto the ground. The length of that projection, denoted $h_{\rm proj}$, verifies:

$$h_{\rm proj} = z_{\rm is} \cos(\alpha_{\rm field}), \tag{A5}$$

with $z_{\rm is}$ the altitude of the sensors and $\alpha_{\rm field}$ the inclination of the field (eq. A1). The angle formed by this projection and the direct path from the shot zone to the infrasound sensors $\alpha_{\rm proj}$ verifies, following straightforward trigonometry and using eq. (A5):

$$\tan(\alpha_{\rm proj}) = \frac{x_{\rm ba} - z_{\rm is}\sin(\alpha_{\rm field})}{h_{\rm proj}} = \frac{x_{\rm ba} - z_{\rm is}\sin(\alpha_{\rm field})}{z_{\rm is}\cos(\alpha_{\rm field})}. \tag{A6}$$

Inserting the aforementioned values, and taking $z_{\rm is}$ as the midpoint between the two sensors, $z_{\rm is} \simeq 85$ m AGL, one obtains:

$$\alpha_{\rm proj} = \arctan\left(\frac{x_{\rm ba} - z_{\rm is}\sin(\alpha_{\rm field})}{z_{\rm is}\cos(\alpha_{\rm field})}\right) \simeq 64.25^\circ. \tag{A7}$$

Since the infrasound sensors carried by the balloon are assumed to hang vertically, their expected angle of incidence for the acoustic wave is the sum of the inclination of the terrain and of the acoustic angle. Consequently, using eqs (A1) and (A7):

$$\alpha_{\rm th,ac} = \alpha_{\rm field} + \alpha_{\rm proj} \simeq 72.87^\circ. \tag{A8}$$